

Phase-Specific Augmented Reality Guidance for Microscopic Cataract Surgery Using Long-Short Spatiotemporal Aggregation Transformer

Puxun Tu¹, Hongfei Ye², Jeff Young³, Peiquan Zhao², Ce Zheng², Xiaoyi Jiang⁴, Xiaojun Chen¹

Abstract—Phacoemulsification cataract surgery (PCS) is a routine procedure conducted using a surgical microscope, heavily reliant on the skill of the ophthalmologist. While existing PCS guidance systems extract valuable information from surgical microscopic videos to enhance intraoperative proficiency, they suffer from non-phase-specific guidance, leading to redundant visual information. In this study, our major contribution is the development of a novel phase-specific augmented reality (AR) guidance system, which offers tailored AR information corresponding to the recognized surgical phase. Leveraging the inherent quasi-standardized nature of PCS procedures, we propose a two-stage surgical microscopic video recognition network. In the first stage, we implement a multi-task learning structure to segment the surgical limbus region and extract limbus region-focused spatial feature for each frame. In the second stage, we propose the long-short spatiotemporal aggregation transformer (LS-SAT) network to model local fine-grained and global temporal relationships, and combine the extracted spatial features to recognize the current surgical phase. Additionally, we collaborate closely with ophthalmologists to design AR visual cues by utilizing techniques such as limbus ellipse fitting and regional restricted normal cross-correlation rotation computation. We evaluated the network on publicly available and in-house datasets, with comparison results demonstrating its superior performance compared to related works. Ablation results further validated the effectiveness of the limbus region-focused spatial feature extractor and the combination of temporal features. Furthermore, the developed system was evaluated in a clinical setup, with results indicating remarkable accuracy and real-time performance, underscoring its potential for clinical applications.

I. INTRODUCTION

Cataract remains the leading cause of blindness worldwide, and phacoemulsification cataract surgery (PCS) has emerged as the established standard of care for its treatment. PCS follows a quasi-standardized procedure involving specific surgical phases [1], enabling the removal of the cataract and the placement of an intraocular lens (IOL) to restore visual acuity. The procedure is typically performed using a surgical microscope, which offers an enhanced view of the surgical field with magnification, brightness, and clarity. However, the success of PCS is highly reliant on the surgical skills of the ophthalmologists, and statistical evidence highlights significant differences in complication

rates among ophthalmologists with varying levels of seniority and experience [2].

In most cases, the surgical microscope used in PCS is equipped with a camera that transmits the surgical field to an external screen, allowing for intraoperative monitoring and procedure recording. The microscopic video contains rich spatiotemporal information, presenting an exceptional opportunity to develop surgical video recognition methods. These methods can extract valuable intraoperative information, such as delineating key anatomical boundaries [3], detecting surgical instruments [4], and computing the rotation [5]. These extracted details can then be overlaid on a 2D/3D screen or the microscopic eyepiece, creating an augmented reality (AR) scene to enhance ophthalmologist’s intraoperative skills [6].

Several intraoperative guidance systems for ophthalmic surgery utilizing microscopic video recognition have been proposed [5], [7], [8]. Despite their clinical significance, certain limitations hinder their implementation in PCS. Firstly, these systems cannot provide phase-specific intraoperative AR information for ophthalmologists, leading to the issue of visual redundancy. In clinical practice, the significance of phase-specific guidance becomes evident, as ophthalmologists hold varying expectations for augmented visual information at different surgical phases. For example, during the incision phase, their focus is on the position of the corneal incision site (Fig. 1 (a)), whereas during the capsulorhexis phase, they prioritize assessing the circular opening range of the capsule (Fig. 1 (b)). If all AR information is provided uniformly across all surgical phases, the presence of redundant visual information could divert their attention and potentially lead to surgical complications. Secondly, existing systems process surgical videos in a frame-wise manner, enabling real-time processing but resulting in the loss of crucial temporal information. These observations motivate us to develop our phasespecific intraoperative guidance system that offers ophthalmologists distinct AR information tailored to different surgical phases.

The key technology in developing the phase-specific AR guidance system is real-time recognition of the surgical phase from microscopic video. While various methods have been proposed for surgical phase recognition [9]-[13], none of them utilizes the recognized surgical phase for intraoperative AR guidance. These methods typically adopt a two-stage framework, with the first stage involving the extraction of spatial features and the second stage employing these features for temporal feature aggregation. The spatial feature extractor is typically trained in a frame-level fashion, where

¹the Institute of Biomedical Manufacturing and Life Quality Engineering, School of Mechanical Engineering, Shanghai Jiao Tong University, China, xiaojunchen@sjtu.edu.cn.

²the Department of Ophthalmology, Xinhua Hospital Affiliated to Shanghai Jiao Tong University School of Medicine, Shanghai, China, zhengce@xinhumed.com.cn.

³the Department of Bioengineering, Rice University, Houston, USA.

⁴the Faculty of Mathematics and Computer Science, University of Münster, Münster, Germany.

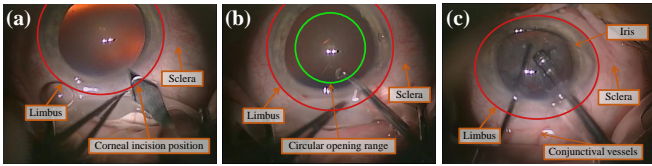


Fig. 1: Three representative surgical phases in PCS: (a) the incision phase, (b) the capsulorhexis phase, and (c) the phacoemulsification phase. Ophthalmologists adjust their focus position according to the different surgical phases. Additionally, the surgical limbus region displays distinct appearances during various surgical phases.

the surgical phase of each frame serves as the ground truth. As the quality of the extracted spatial features plays a crucial role in the temporal aggregation stage, certain methods used hard-frame detection [14] or surgical tools presence supervision [15] to enhance the quality of these spatial features. We observe that there is a substantial variation in semantic features among different phases within the limbus region, whereas the regions outside the limbus region exhibit similar appearances (Fig. 1). These observations motivate us to develop a spatial feature extractor that incorporates supervision from both surgical phase and limbus region, with the objective of obtaining limbus region-focused spatial features.

For temporal feature aggregation, early attempts used Long Short-Term Memory (LSTM) or Gated Recurrent Unit (GRU)-based methods [9], [16] to model the temporal dependencies of spatial features. However, these methods are constrained by their limited temporal receptive field and non-parallel, slow inference. To overcome these limitations, recent studies explored the use of a temporal convolutional network (TCN) or a transformer-based structure, either individually [10] or in combination [12]. These approaches effectively model long-range temporal relationships, leading to improved accuracy and smoother phase recognition. However, globally aggregating temporal features may neglect important local fine-grained information, such as the dynamic interaction between surgical tools and the eye structure. In specific phases of PCS, such as phacoemulsification, the interaction and movement of surgical tools within a short time window play a more prominent role in distinguishing different surgical phases. These observations serve as a motivation for proposing our long short spatiotemporal aggregation transformer (LS-SAT) network. The design is based on the insight that combining spatial features and local temporal features extracted from neighboring frames can provide fine-grained information, while incorporating global temporal features can offer contextual references for accurate recognition of the current frame.

In this study, we developed a novel phase-specific AR guidance system for PCS. The system recognizes the intraoperative surgical microscopic video using the proposed spatiotemporal learning network, which consists of two stages: a multi-task learning stage for limbus segmentation and

spatial feature extraction, and a spatiotemporal aggregation stage for online surgical phase recognition. The segmented limbus region is used for computing guidance parameters and designing AR visual cues. By combining the results of surgical phase recognition, our system offers ophthalmologists a phase-specific AR scene, potentially enhancing their intraoperative skills.

In summary, our major contributions are four-fold:

- We develop a novel phase-specific AR guidance system, which provides the ophthalmologist with distinct visual cues based on the recognized surgical phase. To the best of our knowledge, this is the first-ever system to deliver phase-specific AR guidance for PCS in literature.
- We design a multi-task learning-based spatial feature extractor for extracting limbus region-focused features, facilitating the computation of essential intraoperative guidance parameters based on the limbus boundary and enhancing the effectiveness of spatiotemporal aggregation.
- We propose LS-SAT, a transformer-based spatiotemporal learning network that comprehensively uses spatial features, local temporal features, and global temporal features for accurate surgical phase prediction, making it achieve the state-of-the-art results in a publicly available dataset and an in-house dataset.
- We propose a pipeline for automatically computing the parameters of intraoperative visual cues, which introduces a curvature-based contour points filter to enhance the robustness of limbus ellipse fitting, as well as a regional restricted normal cross-correlation approach for rotation computing.

II. RELATED WORKS

A. AR guided microscopic ophthalmic surgery

Most intraoperative microscopic AR guidance systems [6], [17], [18] utilized an external optical tracker for microscope calibration, patient registration, and pose tracking. In these systems, preoperative surgical planning information was overlaid on the microscopic output video or eyepieces. However, these systems are not applicable to ophthalmic surgeries due to the soft tissue nature of the eyeball, which prevents the fixation of an optical reference frame on it. In ophthalmic surgery, a few works processed the online microscope video to design intraoperative guidance system. Nespolo *et al.* [8] designed a multi-task convolutional neural network (CNN) to locate the pupil and classify the surgical phase, but the recognized surgical phases are not utilized for intraoperative guidance. Zhai *et al.* [5] developed an intraoperative IOL placement guidance system for cataract surgery by detecting the eye center and tracking the rotation. However, guidance information, such as the corneal meridian line and limbus contour, is visualized throughout the entire procedure, leading to a visual redundancy problem. Nespolo *et al.* [19] employed a deep neural network to segment surgical instruments and tissue boundaries in real-time for an image-guided ophthalmic surgery system. Nonetheless, the presence of overlapping visual information unrelated to

phase differentiation can sometimes obstruct the surgeon’s field of vision.

B. Online surgical phase recognition

Early attempts [20] utilized CNN-based networks to predict the current surgical phase on a frame-by-frame basis, but this approach neglected the temporal correlation between frames, resulting in inconsistent phase recognition. Some studies focused on spatiotemporal learning in surgical microscope videos using methods such as 3D CNN [21], LSTM [9], or GRU [16]. However, these methods either suffered from slow inference or had limited temporal receptive fields. Czempiel *et al.* [10] introduced TeCNO, a multi-stage TCN-based network that captures global temporal dependencies of spatial features. However, TCN’s performance on phase-changing frames was not optimal due to the use of temporally invariant kernels. More recent works have employed transformer-based architectures for spatiotemporal aggregation. Czempiel *et al.* [11] proposed OperA, which employed attention-regularized transformers for online surgical phase recognition. Gao *et al.* [12] presented TransSVNet, a hybrid embedding model that combines spatial and temporal features generated from TCN. Zou *et al.* [23] developed an auto-regressive transformer framework that utilizes prediction results from historical frames for current phase recognition. However, the lack of local fine-grained features for spatiotemporal aggregation has limited the performance of these methods, particularly in challenging frames.

III. METHODS

A. System overview

The clinical setup and hardware components of our developed intraoperative AR guidance system for PCS is shown in Fig. 2. A surgical microscope (OPMI Lumera T, Carl Zeiss Meditec AG, Germany) is employed for ophthalmic surgeries. To enable seamless video streaming, a camera adapter (3CMOS, Sony Corporation, Japan) is mounted on the microscope, connecting it to the surgical video capture system (MCC-1000MD, Sony Corporation, Japan). The captured intraoperative video is transmitted to a workstation (Precision 5820-Tower, Dell Technologies Inc., USA), where our proposed spatiotemporal network is deployed for real-time surgical phase recognition and limbus region segmentation, as described in Sec. III. B. Subsequently, the extracted limbus region is used to compute the guidance parameters and the eye rotation parameters, as described in Sec. III. C. This information contributes to design AR visual cues and construct a phase-specific AR scene, promptly displayed on an external screen (T3252U, HKC Corporation, China), thereby enhancing the ophthalmologist’s visual guidance throughout the procedure, as described in Sec. III. D.

This study was approved by the ethics committee of the Xinhua Hospital Affiliated to Shanghai Jiao Tong University School of Medicine (Approval No. XHEC-D-2023-130). It is essential to highlight that this study adheres to the standard of sterile operation for ophthalmic surgery. Furthermore, adhering to clinical ethical boundaries, the implementation

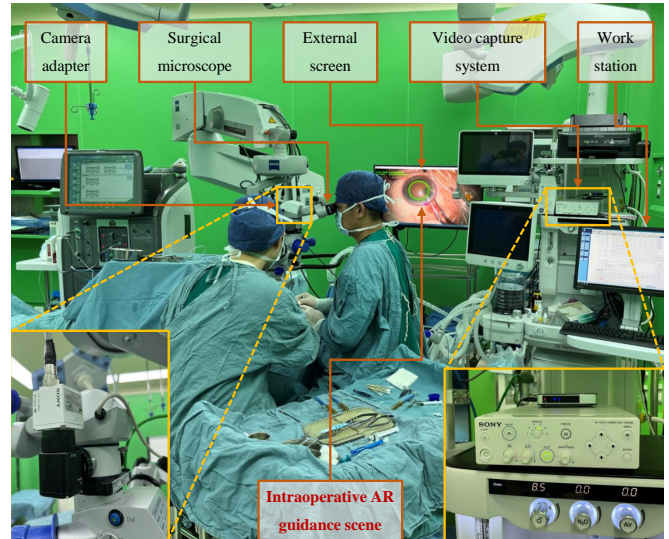


Fig. 2: The clinical setup and hardware components of our developed AR guidance system for PCS.

of the hardware equipment does not interfere with the traditional surgical field or the established practices of the ophthalmologists.

B. Spatiotemporal network for microscopic surgical video recognition

1) *Overview*: Fig. 3 illustrates the architecture of our proposed spatiotemporal network, comprising two stages: the spatial feature extraction stage and the spatiotemporal aggregation stage. The network takes as input a surgical microscope video denoted as $X_t = \{x_1, \dots, x_t\}$, where each frame $x_i \in \mathbb{R}^{H \times W \times C}$, H and W represent the height and width, and $C = 3$ denotes the number of channels. Note that $1 \leq t \leq T$, and T represents the video length. The spatial feature extraction stage (Fig. 3 (a)) is designed as a multi-task learning structure. It maps X_t to a set of spatial features denoted as $S_t = \{s_1, \dots, s_t\}$, where each $s_i \in \mathbb{R}^{2048}$. Besides, the stage also generates a set of segmented limbus regions represented as $E_t = \{\bar{e}_1, \dots, \bar{e}_t\}$, where each $\bar{e}_i \in \mathbb{R}^{H \times W \times C_0}$ and $C_0 = 2$ represents the number of output channels. The spatiotemporal aggregation stage (Fig. 3 (b)) firstly employs a linear layer to reduce the dimension of S_t by a factor of κ , resulting in $S_t^{sf} = \{s_1^{sf}, \dots, s_t^{sf}\}$, where each $s_i^{sf} \in \mathbb{R}^{2048/\kappa}$. Subsequently, the LS-SAT model is utilized to aggregate the global temporal features, local temporal features, and spatial features, producing the surgical phase probability $\bar{p}_t \in \mathbb{R}^{K_s}$, where K_s represents the number of phases.

2) *Limbus region-focused spatial feature extraction*: We designed a multi-task learning structure to jointly train the tasks of limbus region segmentation and spatial feature extraction, instead of training them separately, for two reasons: 1) During PCS, the appearances and surgical tools within the limbus region exhibit significant variations across different surgical phases, while other regions like the sclera tend to have similar semantic features (Fig. 1). By training these two tasks together, the model can effectively capture and

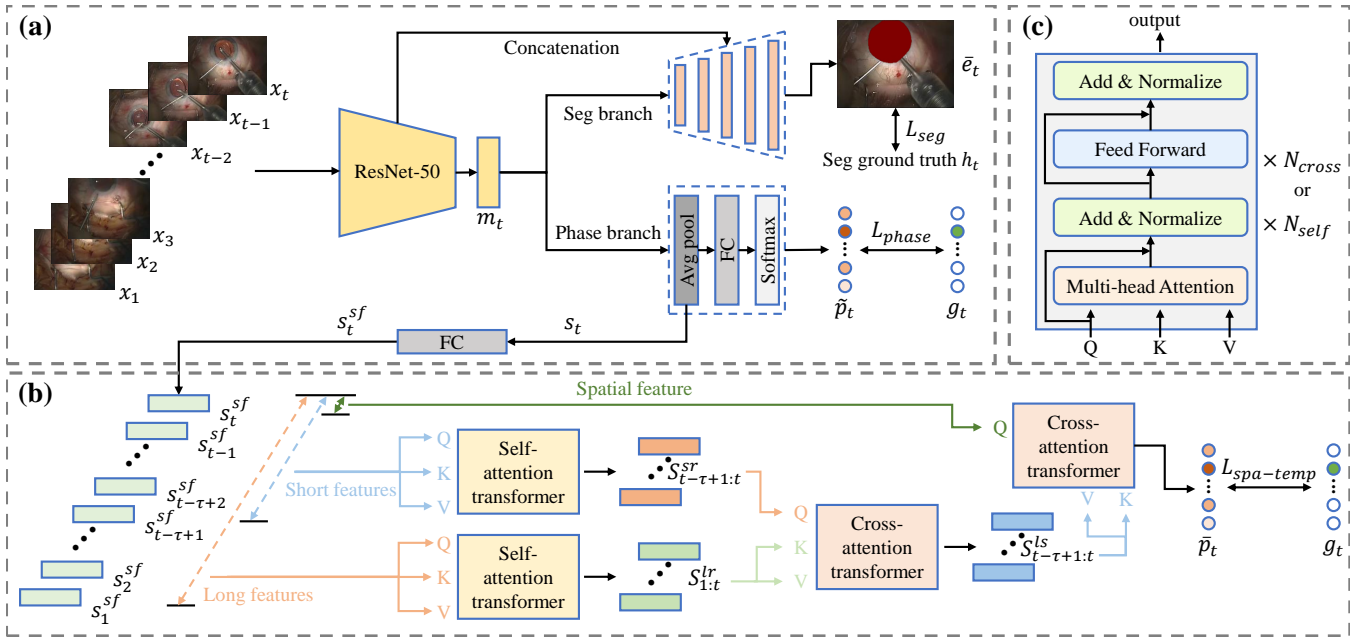


Fig. 3: The architecture of our proposed spatiotemporal aggregation network. (a) The spatial feature extraction stage. (b) The spatiotemporal aggregation stage. (c) The self- and cross-attention module.

leverage the shared semantic information and correlations between them. This enables the model to generate spatial features that are specifically focused on the limbus region, enhancing comprehension of the surgical scene. 2) By sharing the feature extraction parameters between the two tasks, we promote computational efficiency, which is crucial for achieving real-time intraoperative guidance.

Our spatial feature extraction network utilizes ResNet-50 [24] as the backbone, employing hard parameter sharing. For each input frame x_t , the backbone generates an output feature map $m_t \in \mathbb{R}^{H_m \times W_m \times C_m}$, where H_m and W_m represent the height and width, and $C_m = 2048$ represents the number of channels. The feature map is then fed into two branches: the frame-wise phase recognition branch and limbus segmentation branch. The frame-wise phase recognition branch comprises an average pooling layer, a fully connected layer, and a softmax layer. The output of this branch is denoted as $\tilde{p}_t \in \mathbb{R}^{K_s}$, representing the phase probability of x_t . The limbus segmentation branch incorporates a decoder with upsampling and concatenation, resembling the U-net [25] architecture. The output of this branch is $\bar{e}_t \in \mathbb{R}^{H \times W \times C_0}$.

After training the spatial feature extraction stage, we extract the spatial feature s_t for each input frame x_t by taking the output of the average pooling layer in the frame-wise phase recognition branch. These spatial features S_t serve as the input for the subsequent spatiotemporal aggregation stage.

3) *LS-SAT-based surgical phase recognition*: Our LS-SAT network effectively captures both global and local temporal dependencies of the input spatial features. It further aggregates the extracted limbus-region focused spatial features to facilitate online phase recognition. Our network is built upon the transformer architecture [22], which leverages the

attention mechanism to model long-range spatial and temporal interactions in a parallel manner, making it well-suited for surgical video recognition. We utilize the self-attention mechanism to capture temporal dependencies in both short- and long-range spatial features. Given an input spatial feature sequence \bar{S} , the multi-head self-attention module takes it as the Query (Q), Key (K), and Value (V) and can be expressed as

$$\text{SA}(\bar{S}) = \text{softmax}\left(\frac{\bar{S} \cdot \bar{S}^T}{\sqrt{d_{sf}}}\right)\bar{S}, \quad (1)$$

where $d_{sf} = 2048/\kappa$ represents the dimension of \bar{S} . To capture long-range dependencies, we consider all past frames up to time t , referred to as $S_{1:t}^{sf} \in \mathbb{R}^{t \times (2048/\kappa)}$, and take them as \bar{S} . In contrast, for capturing short-range dependencies, we focus on a specific window of τ past frames at time t , denoted as $S_{t-\tau+1:t}^{sf} \in \mathbb{R}^{\tau \times (2048/\kappa)}$, and take them as \bar{S} . We denote the number of self-attention layers as N_{self} , and the outputs of the long-range and short-range self-attention modules as $S_{1:t}^{lr} \in \mathbb{R}^{t \times (2048/\kappa)}$ and $S_{t-\tau+1:t}^{sr} \in \mathbb{R}^{\tau \times (2048/\kappa)}$, respectively.

We aggregate short and long temporal features using a cross-attention module that takes Q and K from different sources. Here, we take the short-range temporal features $S_{t-\tau+1:t}^{sr}$ as Q and the long-range temporal features $S_{1:t}^{lr}$ as K and V. The long-short cross-attention module can be formulated as

$$\text{LS}(S_{t-\tau+1:t}^{sr}, S_{1:t}^{lr}) = \text{softmax}\left(\frac{S_{t-\tau+1:t}^{sr} \cdot S_{1:t}^{lrT}}{\sqrt{d_{sr}}}\right)S_{1:t}^{lr}, \quad (2)$$

where $d_{sr} = 2048/\kappa$ represents the dimension of $S_{t-\tau+1:t}^{sr}$. We denote the number of cross-attention layers as N_{cross} , and the output of the cross-attention module as long-short temporal features $S_{t-\tau+1:t}^{ls} \in \mathbb{R}^{\tau \times (2048/\kappa)}$.

We then aggregate the spatiotemporal features using an

other cross-attention module. We take S_t^{sf} as Q and $S_{t-\tau+1:t}^{ls} \in \mathbb{R}^{\tau \times (2048/\kappa)}$ as K and V, promoting the interaction between the limbus-region focused spatial features and the long-short temporal features. The spatiotemporal cross-attention module can be formulated as

$$\text{ST}(S_t^{sf}, S_{t-\tau+1:t}^{ls}) = \text{softmax}\left(\frac{S_t^{sf} \cdot S_{t-\tau+1:t}^{ls}}{\sqrt{d_{sf}}}\right) S_{t-\tau+1:t}^{ls}. \quad (3)$$

The output of the spatiotemporal cross-attention module is denoted as $\hat{p}_t \in \mathbb{R}^{2048/\kappa}$, which is connected to a fully connected layer, and a softmax layer to produce \bar{p}_t as

$$\bar{p}_t = \text{softmax}(W_p \cdot \hat{p}_t), \quad (4)$$

where $W_p \in \mathbb{R}^{(2048/\kappa) \times K_s}$.

4) *Training*: We define the ground truth for the surgical phase as $g_t \in \mathbb{R}^{K_s}$, and the ground truth for the limbus segmentation as $h_t \in \mathbb{R}^{H \times W \times C_o}$. The spatial feature extraction stage is trained to extract spatial features, which are then utilized to train the spatiotemporal aggregation stage.

The loss function for training the spatial feature extraction stage consists of two parts: the phase recognition part L_{phase} and the limbus segmentation part L_{seg} . We employ cross-entropy loss for L_{phase} , given by

$$L_{phase} = -\frac{1}{K_s} \sum_{s=1}^{K_s} g_{t,s} \log \bar{p}_{t,s}. \quad (5)$$

For L_{seg} , we utilize a hybrid loss of cross-entropy and Dice, expressed as

$$L_{seg} = -\frac{1}{H \times W \times C_o} \sum_{c=1}^{C_o} \sum_{i=1}^{H \times W} \bar{e}_{t,i}^c \log h_{t,i}^c + \alpha \left(1 - \frac{2 \sum_{c=1}^{C_o} \sum_{i=1}^{H \times W} \bar{e}_{t,i}^c h_{t,i}^c}{\sum_{c=1}^{C_o} \sum_{i=1}^{H \times W} \bar{e}_{t,i}^c + \sum_{c=1}^{C_o} \sum_{i=1}^{H \times W} h_{t,i}^c}\right), \quad (6)$$

where α is a weighting coefficient. The loss function of the spatial feature extraction stage is represented as

$$L_{sf} = L_{phase} + \beta L_{seg}, \quad (7)$$

where β is a weighting coefficient.

Due to significant variations in the duration of each surgical step within the dataset, a class-imbalanced problem arises. To address this, we employ a weighted cross-entropy loss during the training of the spatiotemporal aggregation stage, denoted as

$$L_{spa-temp} = -\frac{1}{K_s} \sum_{s=1}^{K_s} w_s g_{t,s} \log \bar{p}_{t,s}, \quad (8)$$

where w_s represents the weight parameter, which is inversely proportional to the phase frequencies [26].

C. Intraoperative guidance parameters computation

The spatiotemporal model is deployed intraoperatively to recognize the surgical phase p_t and obtain the limbus segmentation result e_t . The boundary of the segmented limbus region can be fitted as an ellipse [5][27]. In this study, we leverage the segmented limbus region e_t at a given time t to compute two types of essential intraoperative guidance parameters: 1) the fitted limbus ellipse parameters, including the central coordinates (σ_t^x, σ_t^y) , the lengths of the major and

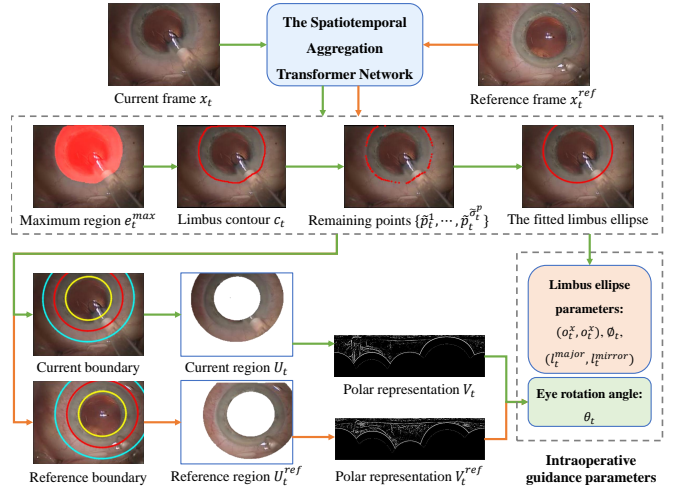


Fig. 4: The pipeline for intraoperative guidance parameters computation.

minor axes $(l_t^{major}, l_t^{minor})$, and the rotation angle of the fitted ellipse ϕ ; 2) the eye rotation angle θ_t , which represents the rotational displacement of the current frame relative to a reference frame.

Based on clinical experience, the parameters of specific intraoperative guidance visual cues, such as the position of the incision curve and the range of the capsulorhexis, can be determined using the fitted ellipse parameters. Additionally, the eye rotation parameters can be utilized to design rotation reference visual cues, which play a crucial role in achieving accurate intraoperative IOL alignment. The computation pipeline of these intraoperative parameters is demonstrated in Fig. 4, and the following sections elaborate on the details of this pipeline.

1) *Fitted limbus ellipse parameters computation*: Firstly, we remove potential mis-segmented regions in e_t by extracting the maximum connected region, denoted as $e_t^{max} = \max\{e_t^1, \dots, e_t^{\sigma_t^e}\}$, where σ_t^e represents the number of regions. We then extract the contour of e_t^{max} , denoted as c_t , to obtain a set of contour points $\{p_t^1, \dots, p_t^{\sigma_t^p}\}$, where σ_t^p represents the number of points. The curvature of each contour point p_t^i can be computed using its neighboring points p_t^{i-1} and p_t^{i+1} , represented as $\ell_t^i = \text{curv}\{p_t^{i-1}, p_t^i, p_t^{i+1}\}$. Next, we define a curvature threshold of μ_{curv} , and exclude the i -th boundary point or outlier when $\ell_t^i < \mu_{curv}$. The remaining boundary points are denoted as $\{\bar{p}_t^1, \dots, \bar{p}_t^{\sigma_t^p}\}$, which can be utilized for fitting the limbus ellipse. The limbus ellipse parametric equation is given by

$$\begin{cases} x_t = \sigma_t^x + l_t^{major} \cos(\varphi) \cos(\phi_t) - l_t^{mirror} \sin(\varphi) \sin(\phi_t) \\ y_t = \sigma_t^y + l_t^{major} \cos(\varphi) \sin(\phi_t) + l_t^{mirror} \sin(\varphi) \cos(\phi_t) \end{cases} \quad (9)$$

We construct an error function representing the sum of squared distances from each remaining boundary point to the fitted ellipse, denoted as

$$E_x = \sum_{i=1}^{\sigma_t^p} ((x_t^i - x_t)^2 + (y_t^i - y_t)^2). \quad (10)$$

TABLE I: The definition of our designed AR visual cues.

AR visual cue	Definition
Fitted limbus contour (FLC)	The fitted limbus ellipse with central coordinates (o_t^x, o_t^y) , the lengths of the major and minor axes $(l_t^{major}, l_t^{minor})$, and a rotation angle ϕ_t .
Primary incision guideline (PIG)	A line starts from (o_t^x, o_t^y) , extending $(l_t^{major} + l_t^{minor}) \times 0.3$, and forming an included angle of 95° with RRL.
Primary incision curve (PIC)	A curve within FPC, having a length equal to the maximum axial distance of the knife, and with PIG serving as the dividing line.
Secondary incision guideline (SIG)	A line starts from (o_t^x, o_t^y) , extending $(l_t^{major} + l_t^{minor}) \times 0.3$, and forming an included angle of 175° with RRL.
Secondary incision curve (SIC)	A curve within FPC, having a length equal to the maximum axial distance of the secondary incision knife, and with the SIG serving as the dividing line.
Capsulorhexis circular range (CCR)	A circle with a diameter of $(l_t^{major} + l_t^{minor})/2$.
Rotation reference line (RRL)	A line passes through (o_t^x, o_t^y) , forming an included angle of θ_t with the horizontal direction, and having a length of $l_t^{major} \times 1.2$.

Finally, the limbus ellipse parameters, including (o_t^x, o_t^y) , $(l_t^{major}, l_t^{minor})$, and ϕ_t can be determined through optimization of the nonlinear least-squares problem utilizing the Levenberg-Marquardt algorithm. In this optimization process, (o_t^x, o_t^y) is initially set to the average of all boundary points, $(l_t^{major}, l_t^{minor})$ is initialized at half the average distance from all boundary points to (o_t^x, o_t^y) , and ϕ_t is initialized to 0.

2) *Eye rotation parameters computation*: For current frame x_t with a predicted surgical phase p_t , we take the first frame of phase p_t as the reference frame x_t^{ref} . Our eye rotation method aims to compute the rotation degree θ_t between x_t and x_t^{ref} .

We observe that regions around the limbus boundary, such as iris and conjunctival vessels, display distinguishable texture features (Fig. 1 (c)). Therefore, our initial step is to limit the computation of rotation near the limbus boundary. We define the restricted region using the parameters $d_t^{in} = (l_t^{major} + l_t^{minor})/2/\lambda_t^{in}$ inside the limbus boundary and $d_t^{out} = (l_t^{major} + l_t^{minor})/2/\lambda_t^{out}$ outside the limbus boundary, where λ_t^{in} and λ_t^{out} represent the scale factors. The restricted region can be expressed as

$$U_t = \{(x_t, y_t) \mid |d_t^{in} \leq \sqrt{(x_t - o_t^x)^2 + (y_t - o_t^y)^2} - (l_t^{major} + l_t^{minor})/2 \leq d_t^{out}\}. \quad (11)$$

Next, we proceed to convert the t -th restricted region U_t and the reference restricted region U_t^{ref} into polar coordinate representations, denoted as V_t and V_t^{ref} , respectively. The rotation between U_t and U_t^{ref} can then be equivalently represented as the displacement between V_t and V_t^{ref} .

To achieve robust displacement estimation, we employ the normalized cross-correlation-based method. The normalized

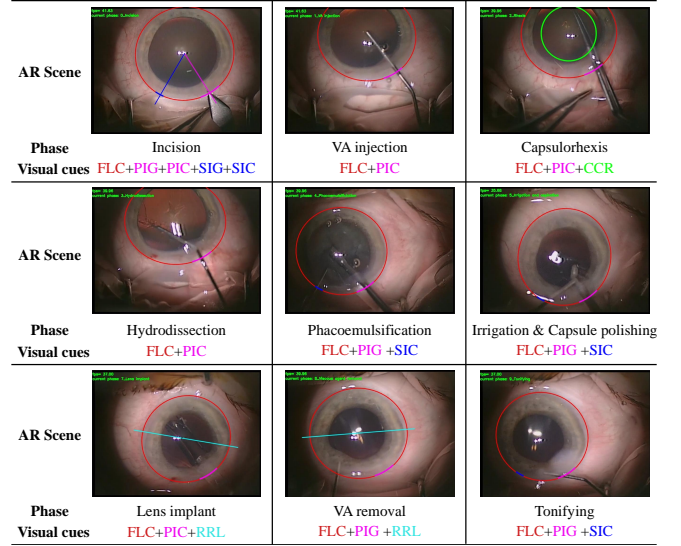


Fig. 5: Phase-specific AR guidance scene. Each scene is superposed with different combinations of visual cues based on the recognized surgical phase. Different AR visual cues are shown with different colors.

cross-correlation between V_t and V_t^{ref} is given by

$$D(u, v) = \sum_{i=1}^{N_{cc}} (V_t^{ref}(x_i, y_i) - \mu(V_t^{ref})) * (V_t(x_i - u, y_i - v) - \mu(V_t)) / (\sigma_t^{ref} * \sigma_t), \quad (12)$$

where $\mu(V_t^{ref})$ and $\mu(V_t)$ represent the mean of V_t^{ref} and V_t . Similarly, σ_t^{ref} and σ_t represent the standard deviation of V_t^{ref} and V_t , respectively. N_{cc} represents the number of pixels in V_t . By solving $\max D(u, v)$, we obtain the displacement (u_{max}, v_{max}) . Subsequently, the displacement is converted into angular representation to obtain the rotation degree θ_t .

D. Phase-specific AR Guidance in PCS

We utilize the intraoperative guidance parameters to design AR visual cues, which are then combined with surgical phase information to provide a phase-specific AR scene for ophthalmologists.

By observing the attention behavior of ophthalmologists during PCS, we have designed seven visual cues in collaboration with ophthalmologists, and their definitions are listed in Table I. Following [1], we divide the PCS into ten phases: incision, viscous agent (VA) injection, capsulorhexis, hydrodissection, phacoemulsification, irrigation, capsule polishing, lens implant, VA removal, and tonifying. We present the AR scene with different combinations of visual cues for each surgical phase in Fig. 5.

IV. EXPERIMENTS AND RESULTS

A. Dataset

Our methods were evaluated on two datasets: 1) Cataract-101 [1], a publicly available dataset for phase recognition in cataract surgery, and 2) XH-CaTa, an in-house dataset from an in-house dataset from the department of ophthalmology,

TABLE II: Comparison results for phase recognition on Cataract-101 and XH-CaTa.

Method	Cataract-101				XH-CaTa			
	Acc (%)	Pre (%)	Rec (%)	Jac (%)	Acc (%)	Pre (%)	Rec (%)	Jac (%)
ResNet-50 [24]	77.7±6.3	75.8±10.3	74.7±9.7	61.3±8.4	75.2±7.5	75.4±7.6	70.4±9.7	57.8±12.1
SV-RCNet [9]	85.8±5.0	83.0±9.2	83.1±8.5	71.1±11.2	83.5±5.0	80.6±6.4	77.4±9.8	66.1±8.3
TMRNet [30]	87.3±7.5	84.9±8.3	83.1±9.4	72.6±6.1	84.0±8.3	77.6±8.8	76.2±7.4	64.5±10.7
TeCNO [10]	89.2±7.4	86.6±8.7	86.2±6.3	76.4±8.6	86.3±7.6	82.9±7.7	82.6±6.9	71.7±9.8
OperA [11]	90.3±4.8	86.8±5.9	85.8±6.9	76.8±9.8	87.7±4.2	85.1±5.3	84.8±6.4	74.2±7.5
Trans-SVNet [12]	91.9±6.9	89.1±4.6	88.4±5.3	80.5±7.7	90.1±4.9	87.5±5.0	85.3±7.0	76.5±9.3
LS-SAT (ours)	93.6±4.3	91.7±5.1	91.1±4.6	84.5±7.3	91.1±4.5	87.8±5.8	87.6±6.5	78.9±6.1

The best results are highlighted with bold font.

Xinhua Hospital Affiliated to Shanghai Jiao Tong University School of Medicine.

Cataract-101 consists of 101 videos with a frame rate of 25 frames per second (fps), and the total duration of the dataset is around 14 hours. Each video was subsampled to 1 fps, and each frame has a resolution of 720×540 pixels. The dataset was annotated into 10 surgical phases. Following [28], we divided the dataset into 73 cases for training and 28 cases for testing, with an additional 13 cases from the training set reserved for validation. XH-CaTa comprises 43 videos with a frame rate of 30 fps, and the total duration of the dataset is around 8.6 hours. Similar to Cataract-101, each video in XH-CaTa was subsampled to 1 fps, and each frame has a resolution of 1920×1080 pixels. XH-CaTa was annotated into 9 surgical phases (irrigation and capsule polishing are considered the same phase) by two experienced ophthalmologists. We used 30 cases for training and 13 cases for testing, with 8 cases from the training set used for validation.

To facilitate limbus region annotation, we employed a larger subsampling rate for both Cataract-101 and XH-CaTa datasets, resulting in a sparser sub-dataset. This approach effectively reduced the annotation workload. The subsampling rate is defined as $\lceil fps \times 10 \times \xi_i \rceil$, where ξ_i represents the normalized reciprocal frequency of the i -th surgical phase. By applying subsampling, each surgical phase in the sub-dataset has an equal number of frames, thereby avoiding the issue of class imbalance during the training of the spatial feature extraction stage. The limbus regions in the sub-dataset were manually delineated by two non-M.D. experts.

B. Implementation Details

We implemented our method in PyTorch, using two NVIDIA GeForce GTX 3090 GPUs. The backbone ResNet-50 [24] was pre-trained on the ImageNet [29] dataset. Each frame was resized to a resolution of 256×256 pixels. Data augmentation strategies including color jitter, random crop and random rotation were applied. The spatial feature extraction stage was trained using the Adam optimizer for 50 epochs. The batch size was set to 256, and the learning rate was set to $5e-5$ for the backbone and $5e-4$ for the segmentation branch and the fully connected layer. The spatiotemporal aggregation stage was trained using the Adam optimizer for 30 epochs, with a batch size of 1 and a learning rate of $1e-4$.

For hyper-parameters, after fine-tuning, we set the dimensional reduction factor $\kappa = 16$, the length of the short window $\tau = 20$, the number of transformer layers $N_{self} = 4$, $N_{cross} = 8$, the weighting coefficient $\alpha=0.6$ and $\beta=0.5$, the curvature threshold $\mu_{curv} = 0.7$, and the scale factors $\lambda_t^{in} = \lambda_t^{out} = 3$.

C. Evaluation of the spatiotemporal aggregation network

1) *Comparisons with state-of-the-art methods:* We compared our LS-SAT network with several state-of-the-art methods in online surgical phase recognition, including 1) ResNet-50 [24], which serves as the backbone of our spatial feature extractor; 2) SV-RCNet [9], a LSTM-based temporal aggregation architecture; 3) TMRNet [30], a memory bank-based long-range temporal aggregation network; 4) TeCNO [10], a multi-stage TCN-based hierarchical refinement network; 5) OperA [11], a transformer-based spatial feature aggregation network; 6) Trans-SVNet [12], a transformer-based spatiotemporal aggregation network. For ResNet-50 [24], SV-RCNet [9], TeCNO [10], TMRNet [30], and Trans-SVNet [12], we implemented them using their open-sourced code. As for OperA [11], we implemented it based on the network architecture and settings described in the original paper. For a fair comparison, we used the limbus region-focused spatial feature for all two-stage-based comparison methods, namely TeCNO [10], OperA [11], and Trans-SVNet [12]. Note that no additional supervision information, such as tool presence or phase remaining time, was employed in any of the methods.

Following [9], [12], we evaluate the performance of surgical phase recognition using four metrics: accuracy (Acc), precision (Pre), recall (Rec) and Jaccard (Jac). The comparison results on both the Cataract-101 dataset and XH-CaTa dataset are listed in Table II. The results demonstrate that our LS-SAT network outperforms all the comparison methods. Notably, when compared to Trans-SVNet, the state-of-the-art method, our method achieves improvements with a margin of 1.7 percentage points (pp) for Acc, 2.6 pp for Pre, 2.7 pp for Rec, and 4.0 pp for Jac on the Cataract-101 dataset. Besides, our method achieves improvements with a margin of 1.0 pp for Acc, 0.3 pp for Pre, 2.3 pp for Rec, and 2.4 pp for Jac on the XH-CaTa dataset.

Additionally, we provide qualitative comparison results using color-coded ribbons in Fig. 6, where each surgical phase is represented by a distinct color. The visualization reveals that our method can achieve a smoother surgical

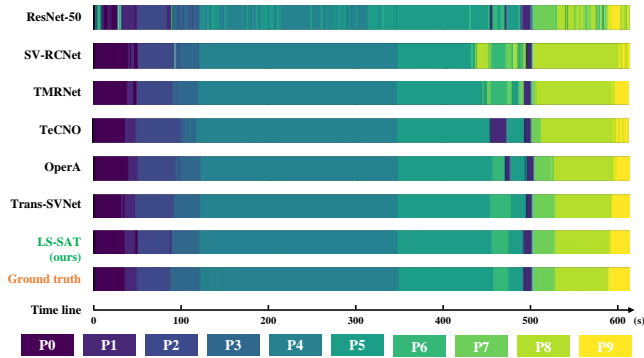


Fig. 6: Qualitative comparison results for a representative case in the Cataract-101 dataset, using different surgical phase recognition methods.

TABLE III: Results of different spatial feature extractor on Cataract-101 dataset.

Stage	Method	Acc (%)	Pre (%)	Rec (%)	Jac (%)	Dice (%)
Stage I	Pha only	77.7±6.3	75.8±10.3	74.7±9.7	61.3±8.4	—
	Seg only	—	—	—	—	93.0±3.3
	Multi	81.9±7.2	79.7±9.5	74.5±8.7	63.1±7.9	94.8±2.8
Stage II	w/o LF	90.1±6.4	86.6±5.6	85.5±5.2	76.6±6.8	—
	with LF	93.6±4.3	91.7±5.1	91.1±4.6	84.5±7.3	—

Stage I: the spatial feature extraction stage; Stage II: the spatiotemporal aggregation stage; LF: limbus-focused.

The best results are highlighted with bold font.

phase prediction and reduce the occurrence of instantaneous erroneous prediction frames.

2) *The effect of the limbus region-focused spatial feature extractor:* We performed an ablation study on the Cataract-101 dataset to evaluate the effectiveness of our proposed limbus region-focused spatial feature extractor. Specifically, we compared the segmentation and surgical phase recognition results obtained by our multi-task feature extractor network with those achieved by the single segmentation network and single surgical phase recognition network. The Dice score was used as the metric for limbus segmentation. Furthermore, we assessed the impact of the quality of the extracted spatial features on the spatiotemporal aggregation stage.

The results are presented in Table III. We observe that the multi-task feature extractor network outperforms the single task-based methods in both surgical phase recognition and limbus segmentation. Moreover, utilizing the limbus region-focused spatial features led to improvements in the spatiotemporal aggregation stage, with an increase of 3.5 pp in Acc, 5.1 pp in Pre, 5.6 pp in Rec, and 7.9 pp in Jac index.

3) *The effect of the long-short spatiotemporal aggregation:* We conducted an ablation study on the Cataract-101 dataset to evaluate the effect of different combinations of long-range temporal aggregation, short-range temporal aggregation, and spatial feature aggregation. The quantitative results, presented in Table IV, highlight that the method combining long features and short features outperforms the methods using each of them individually. Additionally, the

TABLE IV: Results of different feature combination on Cataract-101 dataset.

Long feature	Short feature	Spatial feature	Acc (%)	Pre (%)	Rec (%)	Jac (%)
✓			91.1±5.9	88.0±7.7	87.2±7.1	78.8±8.1
	✓		90.1±6.4	86.6±7.4	85.5±6.0	76.6±8.8
✓	✓		93.1±4.5	90.3±5.8	89.8±4.9	82.8±6.7
		✓	92.1±5.0	88.8±6.3	88.1±6.1	80.4±7.6
✓		✓	91.9±6.2	89.1±6.6	88.4±5.2	80.5±8.2
✓	✓	✓	93.6±4.3	91.7±5.1	91.1±4.6	84.5±7.3

The best results are highlighted with bold font.

TABLE V: Experimental results on clinical cases.

Case	Phase accuracy (%)	Segmentation Dice (%)	Rotation error (°)	fps
1	92.6	93.2	2.6±0.9	37.3±3.4
2	90.8	93.7	2.1±1.3	37.1±3.7
3	94.6	95.4	2.2±0.7	36.4±4.0

incorporation of spatial features in both the long features-based method and the short features-based method yields improved results. Notably, our proposed structure, which combines long-short temporal features and spatial features, achieves the best performance when compared to other combinations.

D. Clinical evaluation of the AR guidance system

1) *Experimental design and setup:* We conducted preliminary clinical experiments to evaluate the performance of our developed AR guidance system for PCS. The experimental setup is depicted in Fig. 2. The model deployed in the clinical experiment was trained on the XH-CaTa dataset. The study involved three clinical cases conducted by a senior ophthalmologist. The results are described below.

2) *Accuracy and real-time performance evaluation:* For each clinical case, we recorded both the original video and AR guidance video. The surgical phase and limbus region in the original videos were manually annotated by an ophthalmologist, serving as the ground truth for microscope video recognition. We compared the intraoperative prediction results in the AR guidance video with the ground truth and calculated the surgical phase recognition accuracy. The qualitative results, including color-coded ribbons for the overall performance and representative AR scenes at different surgical phases shown with green markers, are presented in Fig. 7.

Following [5], we manually annotated evident conjunctival vascular bifurcation landmarks, which were used in conjunction with the limbus central point to compute the rotation ground truth. We compared the predicted rotation results with the ground truth and computed the mean rotation error. Additionally, we recorded the computing time consumption of each frame, including network inference time, guidance parameter computation time, and AR visualization time, and calculated the mean fps of each AR guidance video.

Table V lists the experimental results on clinical cases, which indicate high accuracy in phase recognition, limbus

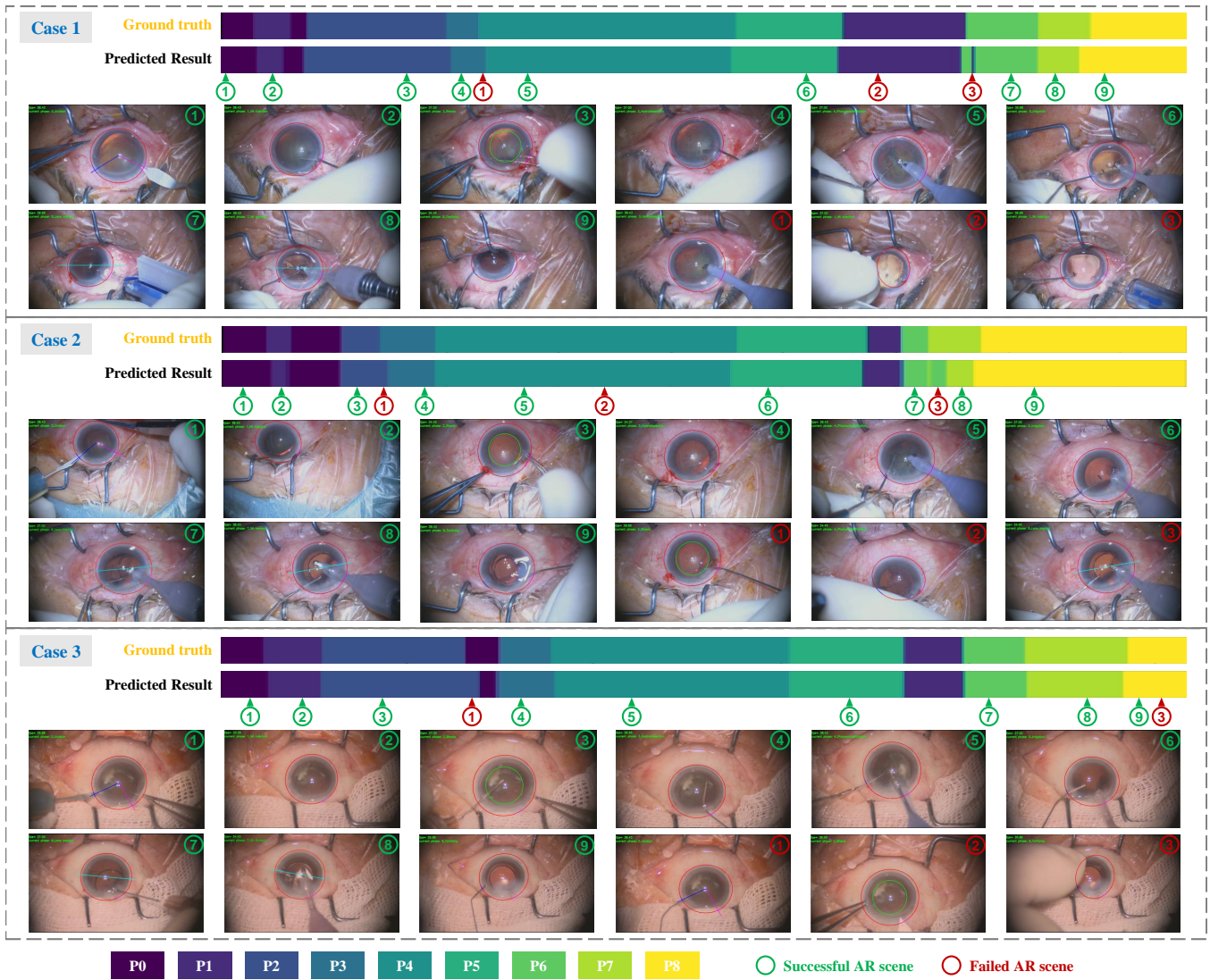


Fig. 7: Intraoperative AR scenes for clinical cases. The inference model deployed is trained on the XH-CaTa dataset. The predicted surgical phase results and ground truth are visually represented using color-coded ribbons. Successful scenes are denoted by green markers, while failed scenes are denoted by red markers.

segmentation and rotation computation. Besides, the fps in each case is higher than 30 fps, meeting the online deployment requirements as the output fps from the video capture system is 30 fps. In clinical practice, we maintained a fixed visualization fps of 30 fps on the external screen.

3) *Failed AR scenes analysis*: We also present some typical failed AR scenes in Fig. 7, indicated by red markers. Our observations reveal that these failed AR scenes commonly occur during phase conversion, when the surgical tools obstruct the surgical field of view, and when motion blur is present in the surgical scene. These failed scenes were primarily caused by either mis-recognition of surgical phases or mis-segmentation of the limbus. In the case of mis-recognition, visual cues that should not appear in a particular phase can be displayed. On the other hand, in the case of mis-segmentation, the intraoperative AR guidance parameters can be miscalculated, resulting in the misalignment of visual

cues.

V. DISCUSSION AND CONCLUSION

In this study, we developed a novel phase-specific intraoperative AR guidance system for PCS. Our system incorporated a spatiotemporal learning network for surgical phase recognition and limbus region segmentation, which were subsequently utilized to calculate the parameters of intraoperative visual cues. By superimposing distinctive AR visual cues corresponding to the recognized surgical phase onto the microscopic video, our system has the potential to enhance ophthalmologists' intraoperative skills.

The experimental results on two datasets demonstrated that our proposed online surgical phase recognition method achieved smoother surgical phase prediction results compared to frame-wise methods [24] and short-range temporal aggregation networks [9], [30]. This outcome is highly

advantageous for the implementation of AR guidance as it prevents potential interference to ophthalmologists resulting from incorrect superposition of visual cues caused by frequent misrecognition of surgical phases. Our method outperformed other long-range temporal aggregation networks [10]-[12] in handling challenging frames, particularly during phase conversion. This elevated effectiveness can be attributed to the combination of short-range temporal features, long-range temporal features, and spatial features. We implemented our spatiotemporal network in a clinical setting to assess the accuracy and real-time performance of our developed AR guidance system for PCS. Our findings indicated that both mis-recognition of surgical phases and mis-segmentation of the limbus can result in failed AR scenes. Specifically, these failed scenes commonly occurred when the limbus region was obstructed or when the video was blurred due to rapid eye or microscope motion. However, it is noteworthy that these erroneous scenarios have limited impact on ophthalmologists as they pertain to non-surgical instrument operation situations.

Nevertheless, our work has some limitations. Firstly, the diversity of surgical instruments and variations in surgical phases across different ophthalmic centers present a challenge in generalizing a model trained on a dataset from one clinical center to be applicable in other clinical centers. In this study, we specifically used the model trained on the XH-CaTa dataset for the clinical validation. By focusing on a single dataset, we aim to provide a more reliable evaluation of our approach in a consistent and controlled setting. Secondly, the use of supervised learning for anatomical segmentation requires manual annotation of the limbus region for each frame sampled from the dataset, which is a labor-intensive task.

In future work, we plan to enhance the AR visualization by directly integrating an AR display device [31] into the eyepieces of the surgical microscope. Additionally, we plan to incorporate tracking and pose estimation of surgical instruments to enable intraoperative AR surgical navigation. Moreover, the application of our AR guidance system, whether through an external display or a direct overlay on the eyepiece, in guiding ophthalmologists during PCS can provide a comprehensive evaluation of its clinical feasibility and potential for widespread adoption.

REFERENCES

- [1] K. Schoeffmann, M. Taschwer, S. Sarny, B. Münzer, M. J. Primus, and D. Putzgruber, "Cataract-101 – Video Dataset of 101 Cataract Surgeries," in *Proc. of the 9th ACM Multi. Sys. Conf.*, 2018, pp. 421-425.
- [2] J. S. Lee, C. H. Hou, and K. K. Lin, "Surgical Results of Phacoemulsification Performed by Residents: A Time-Trend Analysis in a Teaching Hospital from 2005 to 2021," *J. Ophthalmol.*, vol. 2022, pp. 1-6, 2022.
- [3] Z. L. Ni, G. B. Bian, Z. Li, X. H. Zhou, R. Q. Li, and Z. G. Hou, "Space Squeeze Reasoning and Low-Rank Bilinear Feature Fusion for Surgical Image Segmentation," *IEEE J. Biomed. Health Inform.*, vol. 26, no. 7, pp. 3209-3217, 2022.
- [4] H. A. Hajj *et al.*, "CATARACTS: Challenge on automatic tool annotation for cataract surgery," *Med. Image Anal.*, vol. 52, pp. 24-41, 2019.
- [5] Y. Zhai *et al.*, "Computer-Aided Intraoperative Toric Intraocular Lens Positioning and Alignment During Cataract Surgery," *IEEE J. Biomed. Health Inform.*, vol. 25, no. 10, pp. 3921-3932, 2021.
- [6] L. Ma, and B. Fei, "Comprehensive review of surgical microscopes: technology development and medical applications," *J. Biomed. Opt.*, vol. 26, no. 1, pp. 010901-010901, 2021.
- [7] F. Yu, *et al.*, "Assessment of Automated Identification of Phases in Videos of Cataract Surgery Using Machine Learning and Deep Learning Techniques," *JAMA Netw. Open*, vol. 2, no. 4, pp. e191860, 2019.
- [8] R. Garcia Nespolo, *et al.*, "Evaluation of Artificial Intelligence-Based Intraoperative Guidance Tools for Phacoemulsification Cataract Surgery," *JAMA Ophthalmol.*, vol. 140, no. 2, pp. 170-177, 2022.
- [9] Y. Jin, *et al.*, "SV-RCNet: Workflow Recognition From Surgical Videos Using Recurrent Convolutional Network," *IEEE Trans. Med. Imag.*, vol. 37, no. 5, pp. 1114-1126, 2018.
- [10] T. Czempiel, *et al.*, "TeCNO: Surgical Phase Recognition with Multi-stage Temporal Convolutional Networks," in *Proc. Int. Conf. Med. Image Comput. Comput.-Assist. Intervent.*, 2020, pp. 343-352.
- [11] T. Czempiel, M. Paschali, D. Ostler, S. T. Kim, B. Busam, N. Navab, "Opera: Attention-regularized transformers for surgical phase recognition," in *Proc. Int. Conf. Med. Image Comput. Comput.-Assist. Intervent.*, 2021, pp. 604-614.
- [12] X. Gao, *et al.*, "Trans-SVNet: Accurate phase recognition from surgical videos via hybrid embedding aggregation transformer," in *Proc. Int. Conf. Med. Image Comput. Comput.-Assist. Intervent.*, 2021, pp. 593-603.
- [13] W. Yue, H. Liao, Y. Xia, V. Lam, J. Luo, and Z. Wang, "Cascade Multi-Level Transformer Network for Surgical Workflow Analysis," *IEEE Trans. Med. Imag.*, doi: 10.1109/TMI.2023.3265354.
- [14] F. Yi and T. Jiang, "Trans-SVNet: Accurate phase recognition from surgical videos via hybrid embedding aggregation transformer," in *Proc. Int. Conf. Med. Image Comput. Comput.-Assist. Intervent.*, 2019, pp. 449-457.
- [15] Y. Jin, *et al.*, "Multi-task recurrent convolutional network with correlation loss for surgical video analysis," *Med. Image Anal.*, vol. 59, pp. 101572, 2020.
- [16] F. Yi, Y. Yang, T. Jiang, "Not end-to-end: Explore multi-stage architecture for online surgical phase recognition," in *Proc. of the Asian Conf. on Comput. Vis.*, 2022, pp. 2613-2628.
- [17] S. Drouin, *et al.*, "IBIS: an OR ready open-source platform for image-guided neurosurgery," *Int. J. Comput. Assist. Radiol. Surg.*, vol. 12, no. 3, pp. 363-378, 2017.
- [18] I. Cabrilo, K. Schaller, P. Bijlenga, "Augmented reality-assisted bypass surgery: embracing minimal invasiveness," *World Neurosurgery*, vol. 83, no. 4, pp. 596-602, 2015.
- [19] R. G. Nespolo, *et al.*, "Feature Tracking and Segmentation in Real Time via Deep Learning in Vitreoretinal Surgery: A Platform for Artificial Intelligence-Mediated Surgical Guidance," *Ophthalmol. Ret.*, vol. 7, no. 3, pp. 236-242, 2023.
- [20] A. P. Twinanda, S. Shehata, D. Mutter, J. Marescaux, M. de Mathelin, and N. Padoy, "EndoNet: A Deep Architecture for Recognition Tasks on Laparoscopic Videos," *IEEE Trans. Med. Imag.*, vol. 36, no. 1, pp. 86-97, 2017.
- [21] T. Wang, *et al.*, "Intelligent cataract surgery supervision and evaluation via deep learning," *Int. J. Surg.*, vol. 104, pp. 106740, 2022.
- [22] A. Vaswani, *et al.*, "Attention is all you need," in *Proc. Adv. Neural Inf. Process. Syst.*, 2017, pp. 5998-6008.
- [23] X. Zou, W. Liu, J. Wang, R. Tao, G. Zheng, "ARST: auto-regressive surgical transformer for phase recognition from laparoscopic videos," *Comput. Met. in Biom. and Biomed. Eng.: Imag. & Vis.*, vol. 11, no. 4, pp. 1012-1018, 2022.
- [24] K. He, X. Zhang, S. Ren, and J. Sun, "Deep residual learning for image recognition," in *Proc. IEEE/CVF Conf. Comput. Vis. Pattern Recognit.*, 2016, pp. 770-778.
- [25] O. Ronneberger, P. Fischer, T. Brox, "U-net: Convolutional networks for biomedical image segmentation," in *Proc. Int. Conf. Med. Image Comput. Comput.-Assist. Intervent.*, 2015, pp. 234-241.
- [26] D. Eigen, R. Fergus, "Predicting depth, surface normals and semantic labels with a common multi-scale convolutional architecture," in *Proc. IEEE/CVF Conf. Comput. Vis. Pattern Recognit.*, 2015, pp. 2650-2658.
- [27] W. Zhao, Z. Zhang, Z. Wang, Y. Guo, J. Xie, and X. Xu, "ECLNet: Center localization of eye structures based on Adaptive Gaussian Ellipse Heatmap," *Comput. Biol. Med.*, vol. 153, pp. 106485, 2023.

- [28] T. Xia, and F. Jia, "Against spatial-temporal discrepancy: contrastive learning-based network for surgical workflow recognition," *Int. J. Comput. Assist. Radiol. Surg.*, vol. 16, no. 5, pp. 839-848, 2021.
- [29] J. Deng, *et al.*, "Imagenet: A large-scale hierarchical image database," in *Proc. IEEE/CVF Conf. Comput. Vis. Pattern Recognit.*, 2009, pp. 248-255.
- [30] Y. Jin, Y. Long, C. Chen, Z. Zhao, Q. Dou, and P. A. Heng, "Temporal Memory Relation Network for Workflow Recognition From Surgical Video," *IEEE Trans. Med. Imag.*, vol. 40, no. 7, pp. 1911-1923, 2021.
- [31] P. C. Chen, *et al.*, "An augmented reality microscope with real-time artificial intelligence integration for cancer diagnosis," *Nat. Med.*, vol. 25, no. 9, pp. 1453-1457, 2019.